Quantitative HREM observation of the $\Sigma 11(113)/[\bar{1}10]$ grain-boundary structure in aluminium and comparison with atomistic simulation

W. E. KING,* G. H. CAMPBELL,* S. M. FOILES,† D. COHEN‡ & K. M. HANSON§

University of California, Lawrence Livermore National Laboratory, Livermore, CA 94550, U.S.A.

†*Sandia National Laboratories, Livermore, CA 94551, U.S.A.*

‡*University of Minnesota, Department of Chemical Engineering and Materials Science, Minneapolis, MN 55455, U.S.A.*

§*DX-3 Hydrodynamics, Los Alamos National Laboratory, Los Alamos, NM 87545, U.S.A.*

Summary

Quantitative high-resolution electron microscopy (QHREM) involves the detailed comparison of experimental high-resolution images with image simulation based on a model and weighted by the estimated uncertainty in the experimental results. For simple metals, such as Al, models have been systematically improved using nonlinear least-squares methods to obtain simulated images that are indistinguishable from experimental images within the experimental error. QHREM has been used to study the atomic structure of the $\Sigma 11(113)/[\bar{1}10]$ in Al. In this paper, we focus on the method of refining electron-optical imaging parameters and atomic structure to bring the simulated HREM image into agreement with the experimental result to within the experimental error and thus yield a result more useful to the materials scientist. Uncertainties in fitted parameters are studied using the conditional probability distribution function. We discuss experimental results for atomic column locations compared with atomistic simulations of the structure of the grain boundary.

Introduction

The $\Sigma 11(113)/[\bar{1}10]$ symmetric tilt grain boundary has been studied previously by other investigators using high-resolution electron microscopy (HREM) (Mills *et al.*, 1992). In that study, boundary atomic structure was found to be in qualitative agreement with predictions of atomistic simulation. In this study, we quantitatively compare the results of an experimental observation of the $\Sigma 11(113)/[\bar{1}10]$ tilt grain boundary with predictions from atomistic simulations

Correspondence to: Wayne E. King. Tel: 510-423-6547; fax: 510-423-7040; email: weking@llnl.gov

based on the embedded atom method (EAM) and predictions based on more fundamental, local-density approximation (LDA) electronic-structure calculations. This paper focuses on the method of refining electron-optical imaging parameters and atomic structure to bring the simulated HREM image into agreement with the experimental result to within the experimental error and thus yield a result more useful to the materials scientist.

Materials and methods

Sample preparation

High-purity aluminium bicrystals were fabricated using diffusion bonding. Single crystals were orientated by Laue backscatter X-ray diffraction. Specially designed holders allowed the orientated single crystals to be cut on an electric discharge machine (EDM) parallel to the desired crystallographic plane. These surfaces were polished by specially developed flat-polishing techniques (Wien *et al.*, 1996) which maintained the proper crystallographic surface normal and allowed a final polished surface that is flat to within 100 nm. The twist misorientation of the two crystals to be bonded was also set using Laue backscatter X-ray diffraction. To facilitate re-establishment of this orientation prior to bonding, a reference optical flat used for laser alignment was polished on both crystal sides (Wien *et al.*, 1996).

The polished crystals were introduced into an ultrahigh-vacuum (UHV) diffusion bonding machine (King *et al.*, 1993). The polished crystals were mounted on a rotating specimen stage and cleaned by 1 keV Xe^+ ion sputtering at 15° grazing incidence. Removal of surface contaminants was monitored by Auger electron spectroscopy. The crystals were outgassed by heating each individually to 450 °C. This
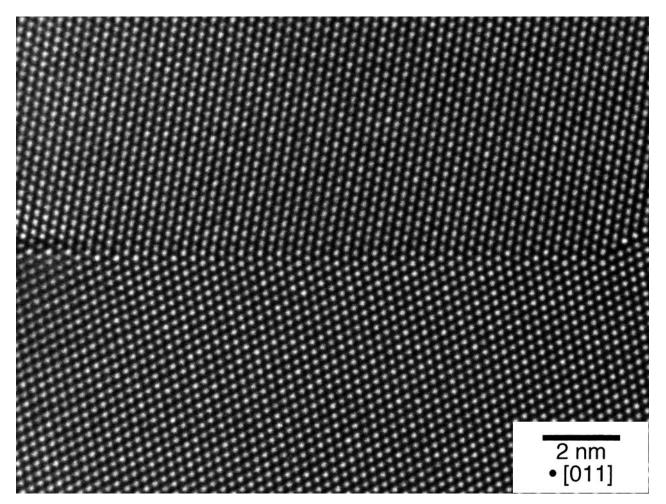
Fig. 1. HREM image of $\Sigma11(113)/[\bar{1}10]$ grain boundary studied in this investigation.

heat treatment also encouraged the segregation of near-surface contaminants. Resputtering, after the heat treatment, created the final, clean surface for bonding. The UHV environment ensured that the cleaned surfaces remained free of contamination for many hours.

Prior to bonding, the crystals were aligned before allowing them to touch. Any contact of the clean surfaces in UHV would result in immediate room temperature bonding. A laser beam reflected from the reference optical flats discussed above allowed for an alignment of $< 0 \cdot 1°$ to be achieved. Once the aligned crystals were brought into contact, a small load of $1 \cdot 0$ MPa was applied. The temperature of the crystals was raised to $600 °C$ and held for 4 h to fully densify the adjoining surfaces to form a single grain boundary.

HREM

The bicrystal was cut by EDM into 300-μm-thick slices with the slice normal orientated along the common $\{110\}$ directions and the grain boundary perpendicular to the surface. The sheets were chemically and mechanically polished to $100\,\mu$m thickness to remove the damaged region resulting from EDM. Three-millimetre-diameter disks for HREM were machined from the sheets using EDM with the grain boundary located near the centre of the disk. The disks were mechanically dimpled $\approx 30\,\mu$m from each side and jet polished using 10% perchloric acid in methanol ($0 \cdot 2$ A, $< - 20\,°C$) until perforation. The samples were given a final thinning using Ar^+ ion sputtering. HREM micrographs were recorded using a JEOL 4000EX transmission electron microscope operated at 400 kV. The HREM images were recorded on electron-optical image film with the beam incident parallel to the $[\bar{1}10]$ direction. Figure 1 shows the image of the grain boundary used in the following analysis. The electron-optical imaging parameters that were measured experimentally or assumed (indicated by asterisk) and held fixed in the analysis are shown in Table 1.

Atomistic simulation

The atomic structure of the boundary was computed using two different theoretical methods which differ in their

Table 1. Electron-optical imaging parameters measured or assumed* in this analysis.

Parameter	Value
Objective aperture diameter	$13 \cdot 1 \, \text{nm}^{-1}$
C_s	$1 \cdot 0 \, \text{mm}$
Focus spread*	$10 \, \text{nm}$
Beam semiconvergence angle	$0 \cdot 91 \, \text{mrad}$
Absorption coefficient*	$0 \cdot 04$

Fig. 2. Calibration curve used to correct for nonlinear response of electron optical image film.

degree of numerical and physical accuracy. The first method used was the EAM which is an empirical model of interatomic interactions. This general framework provides the total energy of the system given a set of atomic coordinates and has been used extensively to compute defect structures in metals (Daw *et al.*, 1993). The particular interactions used here were developed to model Al (Ercolessi & Adams, 1994). The total energy of the system is minimized by relaxing the positions of all of the atoms including any net expansion of the boundary. Also, multiple relative translations of the boundary for the initial state were examined. The structure predicted here is qualitatively similar to the one computed and observed earlier (Mills *et al.*, 1992).

The structure was also computed from *ab initio* electronic-structure calculations. These calculations are based on the local-density approximation to density-functional theory and employed a pseudopotential representation of the electron–ion interaction. The calculations were performed using a mixed basis of plane waves and local atomic-like wave functions as described elsewhere (Foiles *et al.*, unpublished results). The calculations produce the total energy and forces of a periodic supercell containing two grain boundaries separated by $1 \cdot 44 \, \text{nm}$. The dimensions of the cell, or equivalently the net expansion at the boundary, are taken from EAM calculations with the same geometry. The EAM positions are then refined to minimize the LDA energy. The positions were adjusted until the largest force on an atom was reduced from $2 \cdot 5 \, \text{eV} \, \text{nm}^{-1}$ for the EAM positions to less than about $0 \cdot 15 \, \text{eV} \, \text{nm}^{-1}$. The largest change in atomic positions was $0 \cdot 0095 \, \text{nm}$ for the atom in the central plane. It should be noted that this small residual force could lead to numerical errors in the predicted positions. In comparison, for the EAM calculations the corresponding numerical error in the positions is essentially zero. The LDA calculations have the advantage that they represent a much more fundamentally based description of the energetics and are expected to be more physically accurate.

Quantitative HREM

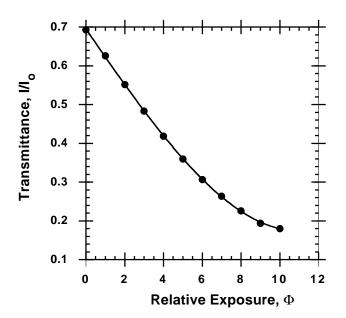Quantitative high-resolution electron microscopy (QHREM) has been used to obtain an estimate of the electron-optical imaging parameters and sample atomic column locations based on the experimental images described above. In this method (King & Campbell, 1993, 1994), nonlinear least-squares algorithms are employed to obtain an optimum fit between an experimental image and an image simulation to within the accuracy of the experimental observation.

Quantitative comparisons require that both the image simulation and the experimental image be in the same units, i.e. that of electrons per incident electron. To accomplish this, regions of interest of a high-resolution micrograph recorded on an electron-optical image film were illuminated by a spherical illuminator and were digitized using a Photometrics $1024 \times 1024 \times 14$-bit CCD array coupled to a Questar QM1 telescope. Image magnifications of $100–200 \, \text{pixels} \, \text{nm}^{-1}$ were used to facilitate comparison of experiment with image simulations and for precise alignment of simulated images with corresponding experimental images. Pixel-to-pixel variations in the gain of the CCD array were corrected by normalization of the image, I, to the flat-field image, I_0, of the illuminator with the electron-optical image film removed. I/I_0 is referred to as the transmittance image. The electron-optical image film was then replaced with a second film containing the image of the unobstructed electron beam. The above procedure was repeated to obtain the transmittance image for the incident electron beam.

The response of the electron-optical image film with increasing electron fluence, Φ, was linearized using the calibration curve shown in Fig. 2. The calibration data were obtained under the same conditions as the experimental data. Typically, transmittances of a high-resolution electron
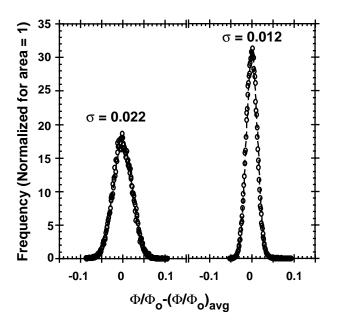
Fig. 3. Statistical distribution of image values about two representative means and fits to normal distributions.

Fig. 4. Standard deviation of the mean image value plotted as a function of image value.

micrograph are in the range $0 \cdot 2 – 0 \cdot 5$. The linearized experimental image, Φ, was normalized by the linearized incident beam flux, Φ_0, to obtain the experimental image in the units of the image simulation.

The next step in the process was to correct the Φ/Φ_0 image for distortions introduced by the projector lens system of the HREM and to align the image with the image simulation. This procedure has been described in detail elsewhere (Campbell *et al.*, 1997). The dominant distortion in the image is due to spiral distortion in the projector lens system. The magnitude of the distortion varies with distance from the centre of the plate and was $\approx 1\%$ for the region investigated in this study.

After the image has been thus prepared, the average and standard deviation images are calculated. The standard deviation image is the pixel-by-pixel standard deviation of the average image calculated using the standard relation.
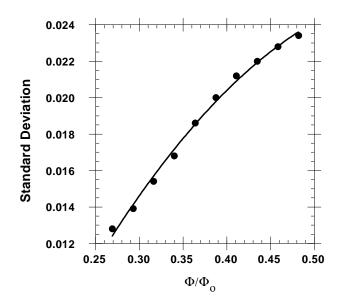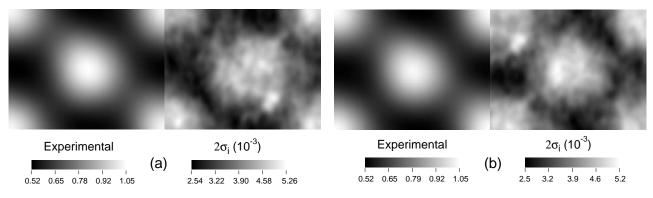
Figure 3 shows the deviation of the experimental data points about their mean value. These deviations were evaluated at each pixel in the average image. The data were grouped into 10 equal bins dividing the intensity range from the minimum to the maximum average value. Data from two representative bins are shown, the one at left from a higher intensity range and the one at right from a lower intensity range. The width parameter (σ) of the fit to a normal distribution for the 10 bins is shown plotted against the midvalue of each bin in Fig. 4.

Averaging provides a method to reduce the contribution from random errors and is an allowable operation on the experimental data (Skilling, 1998). If one makes N independent measurements of the same quantity, then the error at the 95% confidence level is $2\sigma_i^{obs}/\sqrt{N}$, where σ_i^{obs} in this case is the standard deviation image. We refer to $\sigma_i^{obs}/\sqrt{N}$ as simply σ_i. In this work, N measurements of

Fig. 5. Experimental images averaged over ~100 unit cells from either side of the grain boundary in Fig. 1 and corresponding σ_i images.

different unit-cell images were averaged. N was ≈ 100 for the unit-cell images and 5 for the grain-boundary images. This does not correspond strictly to N independent measurements of the same quantity. However, in the image simulation, it is assumed that each unit-cell image in the perfect crystal region is equivalent. This is the origin of the assumption that the N independent measurements are of the same quantity. Any variation in the unit cell images due to systematic errors will make $2\sigma_i$ larger than it would be otherwise. Therefore, $2\sigma_i$ represents an upper-limit estimate for the error. Examples of an average and σ_i image are shown in Fig. 5. The experimentally observed average image is referred to as f_i^{obs}.

For a quantitative fit between experimental and simulated images, we seek to minimize the normalized residual image $R(x)$ at each pixel,

$$R(x) = \begin{pmatrix} r_1(x) \\ r_2(x) \\ \vdots \\ r_k(x) \end{pmatrix} \qquad (1)$$

and

$$r_i(x) = (f_i^{\text{obs}} - f_i^{\text{calc}}(x)) \cdot W_i, \qquad (2)$$

where $f_i^{\text{calc}}(x)$ is the value of the ith pixel in the simulated image based on the s input parameters, x, to the image simulation such as the location of the atomic columns projected along the viewing direction or the electron-optical imaging parameters.

$$x = \begin{pmatrix} x_1 \\ x_2 \\ \vdots \\ x_s \end{pmatrix} \qquad (3)$$

and W_i, the weighting factor, is the quantity that represents the uncertainty associated with measurement of the ith pixel in the experimental image and is taken to be $1/\sigma_i$. The minimization is expressed as

$$\min\left[\sum_{i=1}^{k} r_i(x)^2\right] = \min[\chi^2] \qquad (4)$$

where k is the number of pixels in the image and χ^2 is the well-known chi-squared goodness of fit statistic. Equation (4) is the nonlinear least-squares problem (Moré et al., 1980).

This problem has been addressed in the current work using the MINPACK-1 nonlinear, least-squares optimization code (Moré et al., 1980) coupled with the EMS image simulation code (Stadelmann, 1987). MINPACK-1 employs the Levenberg–Marquardt algorithm (Moré, 1977) to solve the nonlinear least-squares problem. The algorithm relies

on calculation of the Jacobian matrix

$$\left(\frac{\partial r_i(x)}{\partial x_j}\right), \quad 1 \le i \le k, \quad 1 \le j \le s \qquad (5)$$

which is used to correct the initial guess, x_0. Functionally, MINPACK-1 calculates $R(x_0)$ then uses the forward-difference approximation to calculate the Jacobian matrix. The algorithm then estimates a correction, p, to x_0 such that

$$\|R(x_+)\| < \|R(x_0)\|, \qquad (6)$$

where $x_+ = x_0 + p$ and $\|R(x_+)\|$ is the Euclidean norm of R:

$$\|R(x_+)\| = \left(\sum_{i=1}^{k} r_i(x_+)^2\right)^{1/2}. \qquad (7)$$

This procedure is iterated with x_+ replacing x until specific convergence criteria are met. The first criterion is satisfied when the algorithm estimates that the relative error in the sum of the squares of the residuals is less than a specified tolerance. The second criterion is satisfied when the algorithm estimates that the relative error between the best-fit parameters and the actual solution of the problem is less than a specified tolerance. The tolerance is usually set equal to the square root of the single-precision machine parameter. Usually only one of these two criteria is satisfied. A discussion of these criteria can be found in Moré et al. (1980).

Fits were characterized by the chi-squared per degree of freedom goodness-of-fit statistic which has the usual definition

$$\chi_{\text{dof}}^2 = \frac{1}{k-s}\|R(x)\|^2. \qquad (8)$$

We have empirically discovered that there is a constant background contribution to the image. The background is included in the analysis by a modification of Eq. (2),

$$r_i(x) = (f_i^{\text{obs}} - (f_i^{\text{calc}}(x) + b)) \cdot W_i \qquad (9)$$

where b is the background which is included as a free parameter in the optimization procedure. This contribution is critical to the interpretation of the image contrast.

An error exists in the linearization of the film response which appears to be stochastic in nature. The magnitude of this error does not exceed 2% of the experimental image. When averaging is employed, this error dominates the uncertainty in the experimental data. Therefore, W_i was modified to reflect this error as

$$W_i = 1/(\sigma_i + 0 \cdot 02 f_i^{\text{obs}}). \qquad (10)$$

QHREM of grain boundaries is a three-step process: (1) optimization of the electron-optical imaging parameters on an average unit-cell image, (2) optimization of the background contrast and anisotropic imaging parameters (such as beam tilt, crystal tilt, blurring and three-fold astigmatism) on an average grain-boundary image given the results

Table 2. Isotropic imaging parameters optimized based on the images in Fig. 5. χ^2 value is per degree of freedom.
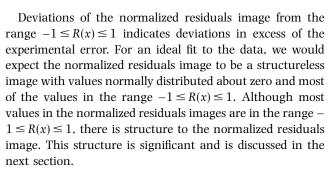
Parameter	Optimum value Side 1	Optimum value Side 2
Defocus (nm)	49·2	51·8
Thickness (nm)	24·1	24·6
Background	0·05	0·06
χ^2_{dof}	0·95	0·25

of step 1 and (3) optimization of the interface atomic structure on the same average grain-boundary image given the inputs from steps 1 and 2. Optimizations were carried out to determine the critical imaging parameters. Once the imaging parameters were established, the optimization of the atomic structure of the grain boundary was carried out.

Results

Electron-optical imaging parameters

In the first step, the isotropic electron-optical imaging parameters of thickness and defocus were optimized based on the images of regions of perfect crystal on either side of the grain boundary in Fig. 5. The results for the optimized parameters are shown in Table 2. Figure 6 shows the averaged experimental image, the best-fit simulation based on the parameters in Table 2 and the normalized residuals image. The comparison of the parameters from either side of the boundary is indicative of their uncertainties. The magnitude of the background contribution was $\approx 5\%$ of the image values.

Deviations of the normalized residuals image from the range $-1 \le R(x) \le 1$ indicates deviations in excess of the experimental error. For an ideal fit to the data, we would expect the normalized residuals image to be a structureless image with values normally distributed about zero and most of the values in the range $-1 \le R(x) \le 1$. Although most values in the normalized residuals images are in the range $-1 \le R(x) \le 1$, there is structure to the normalized residuals image. This structure is significant and is discussed in the next section.

To obtain the best fit to the experimental data, the anisotropic parameters and constant background were also allowed to vary. The multislice calculation of the grain-boundary image assumes that there is no misorientation of the tilt axes of the two crystals, which is of course not the case. The anisotropic parameters deduced in step 1 reflect such differences between the two crystals. Because there is currently no way to account for this in the multislice simulation when the structure of the grain boundary is being optimized, one must find more representative, 'average', anisotropic parameters and background to apply to the structure determination. These parameters are determined in step 2 of the optimization process.

Degrees of freedom

Usually, noise is assumed to be Gaussian and uncorrelated. However, the normalized residuals of Fig. 6 indicate that there is a correlation among the residuals in these images. If we assume that this correlation is not due to deficiencies in the model, we conclude that the number of degrees of freedom is significantly less than the number of pixels in this image. (This assumption is required to continue the analysis. It is recognized that the periodic structure in the
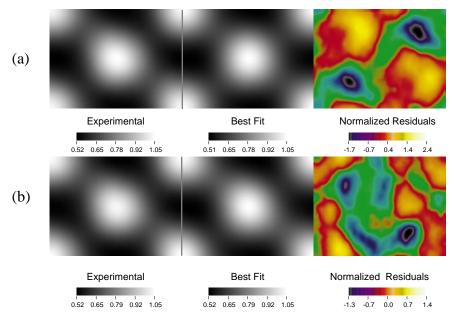

Fig. 6. Average experimental image, best fit image and normalized residuals image from the images (a) side 1 and (b) side 2 in Fig. 5 respectively.
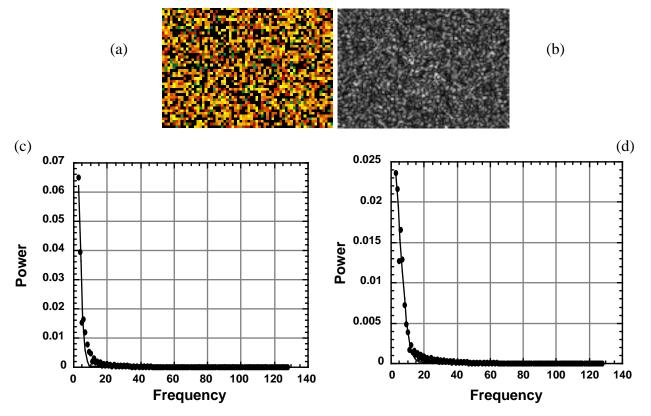
Fig. 7. (a) Image of normally distributed noise about 0 with standard deviation of 1. (b) power spectrum of (a). (c) and (d) Radially averaged power spectra of the normalized residuals images from side 1 and side 2 of the grain boundary in Fig. 6 respectively.

residuals of Fig 6 reveals that some systematic uncertainties in the model remain. However, these uncertainties are rather small, $\leq 2\sigma_i$, and further work is required to fully characterize and include then in the analysis.) The number of degrees of freedom impacts the calculation of χ^2 and the estimation of the uncertainty in the parameters (discussed below). Figure 7(a) shows what the normalized residuals image of Fig. 6 would look like if the residuals were normally distributed about 0 with a standard deviation of 1. (This image was generated using a normally distributed, floating-point, pseudorandom number generator with a mean of zero and a standard deviation of 1.) If we look at Fig. 7(b), we see that corresponding power spectrum is essentially constant to the Nyquist frequency. A standard approach for determining if data are properly sampled is to observe the Fourier transform of the normalized residuals and identify the sampling rate above which no further useful information is available. The normalized residuals from Fig. 6 were Fourier transformed after being padded around the perimeter with an average contrast level region, doubling the image dimensions. Figure 7(c,d) show the radial average of the power spectra for the residuals in Fig. 6. Note the significant difference between these and the power spectrum in Fig. 7(b). The data in Fig. 7(c,d) were fit with Gaussians. We have taken the number of pixels

encompassed by the width of this peak at quarter height divided by four (accounting for the padding) as a measure of the number of degrees of freedom (dof) for the images in Fig. 6. The results are 20 dof for Fig. 6(a) and 37 dof for Fig. 6(b). These results are significantly less than the number of pixels in these images (64×45). The difference between the number of degrees of freedom for Fig. 6(a,b) reflects slight differences in contrast on either side of the boundary evident in Fig. 1.

Anisotropic parameters

In the second step of the optimization process, anisotropic imaging parameters and background contrast, b in Eq. (9), are varied to obtain a best fit with the experimental data. The experimental data for this step are the average and standard deviation images from the entire grain boundary (the whole of Fig. 8). For this optimization, the weighting factor, W_i, was set to zero in the neighbourhood, $\pm 0 \cdot 43$ nm, of the grain boundary so that the fit was to the perfect crystal region, unaffected by the details of the interface atomic structure. The following parameters were optimized: centre of the Laue circle (two parameters), blurring function which accounts for sources of image blurring such as sample vibration and the modulation
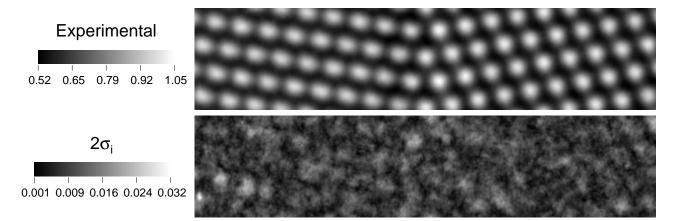
Fig. 8. Average image (top) standard deviation image at bottom from Fig. 1.

transfer function of the CCD array (two parameters), three-fold astigmatism (two parameters), and a constant background contrast (one parameter). The isotropic parameters from Table 2 were used as input to this optimization. The background was allowed to vary. The results of this optimization are shown in Table 3.

In analogy with Fig. 6, the normalized residuals for this step were also found to be correlated. We have measured the number of degrees of freedom using the same procedure described above. The radial average power spectrum for the normalized residuals from this step are shown in Fig. 9. This power spectrum differs from those in Fig. 7 in that it appears to be the sum of two Gaussians, one corresponding to the periodicity of the lattice which appears in the residuals (and is not a random noise) and one extending to higher frequencies. The cutoff for this power spectrum was selected at 40 pixels corresponding to 1256 degrees of freedom. This is also smaller that the number of data points for this image (512×113).

Table 3. Anisotropic imaging parameters and background contrast deduced from analysis of images in Fig. 8.

Parameter	Optimum value
h-centre of the Laue circle	$-0 \cdot 112 \pm 0 \cdot 002$ mrad
k-centre of the Laue circle	$-0 \cdot 334 \pm 0 \cdot 002$ mrad
Θ-centre of the Laue circle*	$-0 \cdot 354$ mrad
x-blurring function	$-0 \cdot 0517 \pm 0 \cdot 0003$ nm
y-blurring function	$-0 \cdot 0444 \pm 0 \cdot 0003$ nm
Angle three-fold astigmatism	$53 \cdot 1 \pm 0 \cdot 8°$
Magnitude three-fold astigmatism	423 ± 36 nm
Background contrast	$0 \cdot 0467 \pm 0 \cdot 0008$
χ^2_{dof}	$1 \cdot 539$

* Obtained by combining h and k results.

One can probe the uncertainties in these parameters by investigating the probability distribution (Skilling, 1998)

$$\Pr(D \,|\, x) = \text{likelihood function} \quad (11)$$

where '|' means 'conditional upon'. When noise is additive and Gaussian, the likelihood function is related to χ^2 by

$$\Pr(D \,|\, x) = Z^{-1} \exp(-\chi^2/2) \quad (12)$$

where

$$Z = \Pi (2\pi/W_i^2)^{1/2}. \quad (13)$$

Figure 10 gives the probability distribution, $Pr(D \,|\, x)$, as a function of each parameter in step 2. Each curve is normalized so that the integral equals 1, consistent with the definition of a probability distribution function. These are referred to as conditional probabilities because all
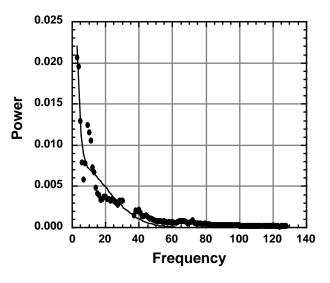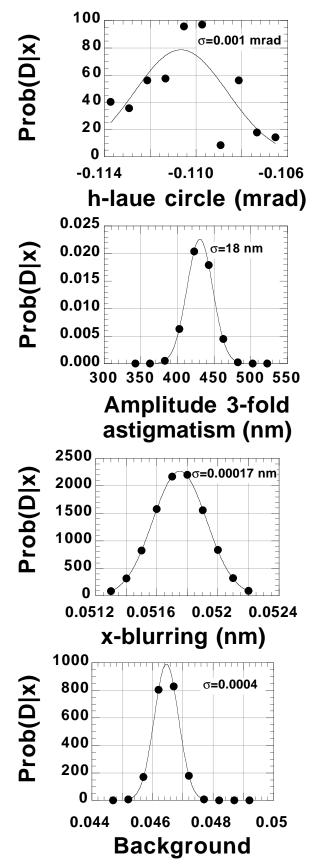

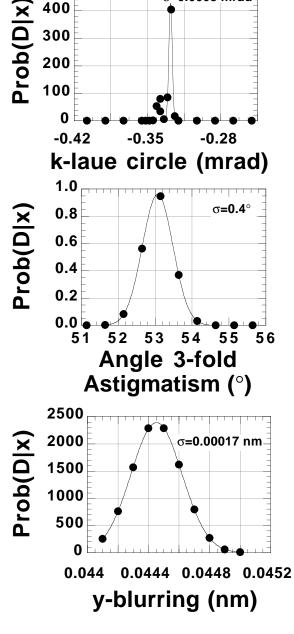**Fig. 9.** Radially averaged power spectrum from normalized residuals image in step 2 of optimization process.

Fig. 10. Prob($D|x$) data for the anisotropic imaging parameters of Table 3.
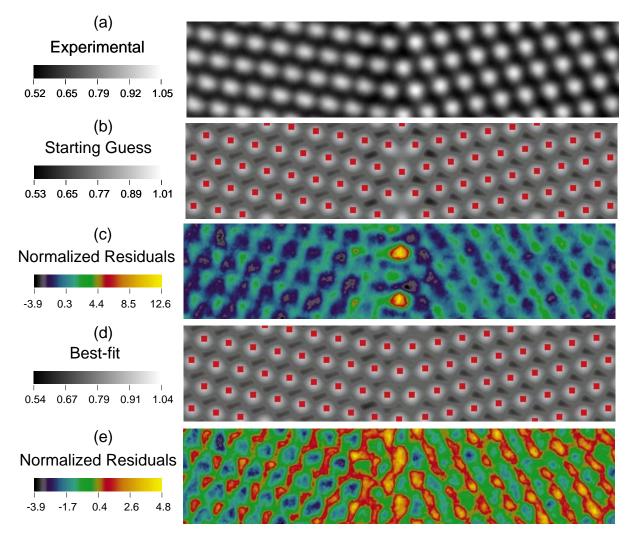
Fig. 11. (a) Experimental image, (b) simulation based on structure predicted by EAM (shown as red squares), (c) normalized residuals corresponding to (b). (d) Best fit image after optimization based on optimized structure (shown as red squares), (e) normalized residuals corresponding to (d).

parameters but one are held fixed at their optimum value. Uncertainties in the parameters, which are considered to be underestimates, can be read directly from these plots. All of the conditional probability distributions are Gaussian distributed except for h-Laue circle and k-Laue circle, the crystal tilts. The data for h-Laue circle and k-Laue circle are not as clear as other data owing to the fact that crystal tilt also causes a shift in the image that must be accounted for in the optimization. Consequently, the curves are not as smooth as for those parameters where no shift is required. Error bars indicating a 95% confidence level are given in Table 3 for all parameters.

Grain-boundary structure

In the third step of the optimization process, the atomic structure of the grain boundary was optimized. Specifically,

atoms within ± 0.43 nm of the boundary were free to move. Atoms to the left of this region were grouped and likewise atoms to the right of this region were grouped. The atoms within each group were held fixed with respect to each other but the group was free to move in the optimization. The starting guesses for the optimization were the atomic column locations predicted from (1) the EAM simulations, and (2) the geometrical or coincident site lattice (CSL) model.

Figure 11 shows (a) the average experimental image, (b) the simulated image based on the atomic structure predicted by the EAM and (c) the normalized residuals image. Regions where the normalized residual image deviates from the range $-1 \leq R(x) \leq 1$ indicate disagreements in excess of the experimental error. Such a disagreement is observed near the two atom locations on the boundary plane of the computation cell. The largest values of the normalized residuals indicate that the contrast
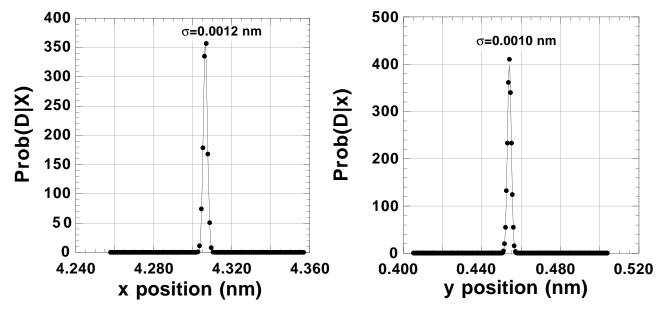
Fig. 12. Conditional probability distribution functions for the atom at the centre of the boundary that moves most in the optimization.

predicted from the model is roughly 13 times outside of the experimental error.

Figure 11 next shows (d) the simulated image based on the optimized atomic structure with the atomic column locations shown and (e) the normalized residuals image. It can be seen that the deviations observed in Fig. 11(c) have been significantly reduced in Fig. 11(e). The value for χ^2_{dof} resulting from this optimization is 1·69. The rigid body lattice translations that represent the difference between the starting (EAM) and ending (best fit) locations of the rigid blocks of atoms to the left and right of the grain boundary were $x = 4·41 \times 10^{-3}$ nm and $y = -4·43 \times 10^{-4}$ nm and $x = 1·49 \times 10^{-3}$ nm and $y = 1·01 \times 10^{-3}$ nm, respectively.

A rough measure of the uncertainty in the estimation of the atomic column locations was obtained by looking at the symmetry of the computational cell. The experimental image of Fig. 8 is periodic along the boundary plane. In fact, two periods of the repeat unit are seen in the average experimental image. Therefore, the results of the atomic column locations contain redundant information which can be used as an estimate of the uncertainty in the atomic column locations. Fourteen atomic columns were free to move in the optimization. By symmetry, only seven of these are unique. Therefore the seven atomic column locations in the top half of the computational cell were compared with those in the lower half of the computational cell. The average displacements of corresponding atoms were calculated. The result is 0·0043 nm. The same procedure was followed for the refined atomic column locations where the starting locations were given by the simple geometric construction (CSL) of the boundary. For this case the result

was 0·0042 nm. These results have been combined to yield an uncertainty of 0·0042 nm.

The conditional probability distribution function has been calculated for the atom on the grain-boundary plane that is shifted most in the optimization. $Pr(D|x)$ is shown in Fig. 12(a) for shifts in x (perpendicular to the grain boundary) and in Fig. 12(b) for shifts in y (parallel to the grain boundary). The uncertainties at the 95% confidence level for displacement in both the x- and y-directions is 0·002 nm which is consistent with the estimates obtained from symmetry arguments above.

Discussion

The imaging parameters necessary for quantification of the atomic structure were determined by nonlinear least-squares fitting methods. The results for thickness and defocus are consistent with estimates based on visual observation of a thickness defocus map. The results are consistent from perfect crystal regions on either side of the grain boundary. The anisotropic imaging parameters have been determined using the same approach. Investigation of the conditional probability distribution function indicated the uncertainties in the parameters.

A low-frequency correlated noise exists in the normalized residuals images of both the unit cells and the grain-boundary images. This correlated noise effectively reduces the number of degrees of freedom in the analysis by a factor of ≈ 40. This reduction is based on the assumption that at this level of degrees of freedom, the noise is uncorrelated. This assumption could be revised if it is found that there is a deficiency in the model which gives rise to the correlated residuals.
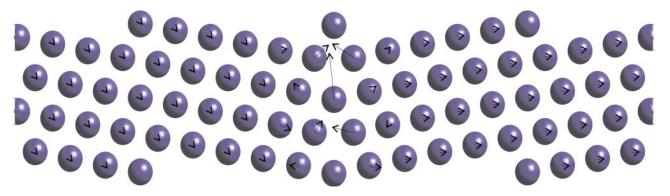
Fig. 13. Vectors (10× magnification) indicating atom shifts from EAM positions due to optimization.

There is a statistically significant difference between the image predicted based on the EAM structure and the experimental image. One way that this difference can be resolved is by optimization of the atomic structure. Figure 13 shows the magnitude of the atomic shifts relative to the EAM prediction, magnified by a factor of 10, required to bring the simulated image into closer agreement with the experimental result. Although several atoms moved from the EAM positions, the dominant atomic shift that was required was an ≈ 0·03 nm shift of the atom at the centre of the grain boundary toward the top of the image. A rough estimate of the uncertainty in the atomic column locations based on symmetry is 0·0042 nm. The estimate for the uncertainties in the position of the central atom was obtained from calculation of $Pr(D|x)$ and is 0·002 nm, consistent with the deduction from symmetry considerations. The shift required to bring the simulation into agreement with the experiment is one order of magnitude larger than the experimental uncertainties.

It is interesting to characterize the local atomic structure surrounding this atomic column. Notice that this atomic column is surrounded by six nearest-neighbour columns. Table 4 summarizes the environment of this atomic column. Entries in the table exist for the three methods: EAM, LDA

and experiment. The six nearest-neighbour columns span the table. For each method, the first row of the table gives the separation of the central atomic column from the indicated atomic column (in units of fractional lattice constants) and the second row for each atom is the angle of the bond relative to the boundary plane (where 0° corresponds to a vector pointing in the negative y-direction). The largest difference between the EAM and the LDA results is the position of the central atom. The sense of the difference between the LDA and EAM is the same as that between the experiment and the EAM. However, the magnitude of the shift predicted by the LDA is smaller than observed experimentally.

Conclusions

This work shows that at least for simple metals such as Al, it is possible to make a quantitative comparison between HREM images and image simulation. Furthermore, it is possible to use fitting methods such as nonlinear least squares to obtain an optimum fit of the simulation with the experiment. Since the experimental image values are normally distributed, the standard deviation of the mean is an acceptable estimate in the uncertainty of the image

Table 4. Summary of distances and angles between the central atom (●) and six neighbouring atoms normalized to the lattice constant for the results from EAM, LDA, and the experimental results. Angles are measured with respect to the vector in the boundary plane pointing between atoms A and F.

	A	B	C	D	E	F
EAM (dist)	0·620	0·621	0·734	0·734	0·621	0·620
EAM (angle)	32·9	101·6	152·7	− 152·7	− 101·6	− 32·9
LDA (dist)	0·634	0·622	0·714	0·714	0·622	0·634
LDA (angle)	31·6	99·3	152·3	− 152·3	− 99·3	− 31·6
Exp. (dist)	0·66 ± 0·01	0·61 ± 0·01	0·67 ± 0·01	0·68 ± 0·01	0·63 ± 0·01	0·66 ± 0·01
Exp. (angle)	28·8 ± 1·7	96·2 ± 1·9	153·0 ± 1·7	− 152·8 ± 1·7	− 95·6 ± 1·8	− 27·9 ± 1·7

```
  D  C
E  ●  B
  F  A
```

value. Knowledge of these uncertainties and other systematic errors are essential for a properly weighted fit to the experimental data. Averaging can be used to reduce random errors. From the optimization, it is possible to obtain estimates of the isotropic and anisotropic imaging parameters and then the atomic column locations. Estimates of the uncertainty in the parameters can be obtained from plots of $Pr(D|x)$ as a function of the parameters.

Results for atomic column locations were compared quantitatively with atomistic simulations of the structure of a $\Sigma11(113)/[\bar{1}10]$ grain boundary in Al using EAM potentials and LDA methods. There is a statistically significant difference between the experimental image and the simulated image based on the EAM. The LDA is found to be in closer agreement with the experiment than the EAM.

Acknowledgments

References

Campbell, G.H., Cohen, D. & King, W.E. (1997) Data Preparation for Quantitative High Resolution Electron Microscopy. *Microsc. Microanal.* **3**(4).

Daw, M.S., Foiles, S.M. & Baskes, M.I. (1993) The embedded-atom method: A review of theory and Applications. *Mater. Sci. Rep.* **9**, 251–310.

Ercolessi, F. & Adams, J.B. (1994) Interatomic potentials from first-principles calculations: the force matching method. *Europhys. Lett.* **26**, 583–588.

King, W.E. & Campbell, G.H. (1993) Determination of thickness and defocus by quantitative comparison of experimental and simulated high-resolution images. *Ultramicroscopy,* **51**, 128–135.

King, W.E. & Campbell, G.H. (1994) Quantitative HREM using non-linear least-squares methods. *Ultramicroscopy,* **56**, 46–53.

King, W.E., Campbell, G.H., Coombs, A.W., Johnson, G.W., Kelly, B.E., Reitz, T.C., Stoner, S.L., Wien, W.L. & Wilson, D.M. (1993) Interface science of controlled metal/metal and metal/ceramic interfaces prepared using ultrahigh vacuum diffusion bonding. *Joining and Adhesion of Advanced Inorganic Materials* (ed. by A. H. Carim, D. S. Schwartz and R. S. Silberglitt), Vol. 314, pp. 61–67. Materials Research Society, Pittsburgh, PA.

Mills, M.J., Daw, M.S., Thomas, G.J. & Cosandey, F. (1992) High-resolution transmission electron microscopy of grain boundaries in aluminum and correlation with atomistic calculations. *Ultramicroscopy,* **40**, 247–257.

Moré, J.J. (1977) *Lecture Notes in Mathematics* (ed. G. A. Watson), pp. 116. Springer-Verlag, Berlin.

Moré, J.J., Garbow, B.S. & Hillstrom, K.E. (1980) *User Guide for MINPACK-1.*

Skilling, J. (1998) Probabilistic data analysis; an introductory guide. *J. Microsc.* **190**, 28–36.

Stadelmann, P.A. (1987) EMS – a software package for electron diffraction analysis and HREM image simulation in materials science. *Ultramicroscopy,* **21**, 131–146.

Wien, W.L., Campbell, G.H. & King, W.E. (1996) Preparation of specimens for use in fabricating bicrystals by UHV diffusion bonding. *Microstruct. Sci.* **23**, 213–218.